Three-Dimensional Numerical Simulation of Ice Accretion on Rotating Components of Engine Entry

FU Zaiguo[1*], *FENG Wenjie*[1], *WANG Zijing*[1], *LIU Bin*[2]

1. College of Energy and Mechanical Engineering, Shanghai University of Electric Power, Shanghai 201306, P. R. China;
2. School of Aeronautics, Northwestern Polytechnical University, Xi'an 710072, P. R. China

(Received 27 March 2023; revised 3 November 2023; accepted 4 November 2023)

Abstract: The rotating engine components subject to Coriolis and centrifugal forces exhibit distinctive ice accretion characteristics when an aircraft operates under supercooled large droplet conditions. This study establishes the mathematical model of the ice accretion on rotating components of engine entry and considers the dynamic characteristics of terminal velocity, deformation, breakup, splash, and rebound of supercooled large droplets. The multiple reference frame method is employed to deal with the fluid flow and heat transfer under the rotating condition. A three-dimensional numerical simulation is conducted to investigate the droplet impingement and ice accretion characteristics of entry components, including the inlet lip, spinner, and fan blades. The simulation results at rotational speeds of 0, 2 000, and 4 100 r/min show that the ice accretion on the inlet lip moves towards the outer surface of the inlet lip from the inner surface as the rotational speed increases. Moreover, the ice accretion on the blades is mainly concentrated at the blade root, and the ice accumulation decreases with the increase of rotational speed. The ice thickness on the inlet lip and spinner increases with increased rotational speed. The maximum ice thickness on the inlet lip and spinner under the rotational speed of 4 100 r/min increases by 0.27 and 2.46 times, respectively, compared to the stationary condition. This work can serve as a reference for developing subsequent anti/de-icing technology.

Key words: aero-engine; 3D icing prediction; supercooled large droplets; rotating blade; numerical simulation

CLC number: V231.1 **Document code**: A **Article ID**: 1005-1120(2023)06-0663-15

0 Introduction

In the process of traversing supercooled droplet clouds, aircraft may be subject to severe icing. Unlike aircraft wing icing, aero engines are extra sensitive to changes caused by ice accretion. Even slight mass accumulation of ice accretion can lead to mechanical damage, and in extreme cases, it can also cause engine flameout, posing a severe hazard to flight safety[1]. Icing accidents account for the highest proportion of aviation accidents caused by hazardous weather conditions, reaching up to 35.4%, with up to more than 2 220 fatalities[2]. In this light, the aviation industry has increasingly employed numerical simulations to assist in airworthiness certification processes. Predicting engine inlet component icing conditions via numerical simulations can provide a reference for anti/de-icing technology. Eliminating the likelihood of engine stall caused or other adverse events by ice accretion will enhance flight safety.

The complexity of engine structure poses challenges for experimental and computational efforts to understand and mitigate engine icing. Researchers have traditionally focused on individual components as study objects to address these challenges. For instance, Papadakis et al.[3] conducted experiments on a full-scale engine inlet to explore the characteristics of ice accretion resulting from supercooled droplets

*Corresponding author, E-mail address: fuzaiguo@shiep.edu.cn.

How to cite this article: FU Zaiguo, FENG Wenjie, WANG Zijing, et al. Three-dimensional numerical simulation of ice accretion on rotating components of engine entry[J]. Transactions of Nanjing University of Aeronautics and Astronautics, 2023, 40(6): 663-677.

http://dx.doi.org/10.16356/j.1005-1120.2023.06.004

at the leading edge of the engine inlet. Similarly, numerical simulations have typically employed single components such as inlet guide vanes, engine inlets, or spinners as the object of calculation[4-6]. Yang et al.[7] developed a complete three-dimensional method for icing prediction and investigated the icing conditions during the takeoff and initial climb phases of a nacelle.

Due to the presence of the rotational component in engines, the fluid flow and heat transfer during rotation are different from those in stationary conditions. To this end, researchers have employed experiments to explore the complex phenomena of engine icing. The rotating spinners[8-9] and fan blades[10] were the main objects of experimental research. For example, Zhang et al.[11] performed the ice wind tunnel experiments on the scaled rotating cone models under different conditions to verify the icing scaling law of rotating cones. Under rime icing condition, the overall ice thickness was uniform, and the ice shape was regular. In contrast, under glaze icing condition, the ice surface was uneven and the ice accumulation was thicker than that in rime icing condition. Li et al.[12] conducted experimental research on the dynamic icing process on three shapes of rotating spinners and investigated the detrimental effects of icing on the engine's inflow. They observed that the shape of the spinner significantly influenced ice mass, icing area and needle-shaped icicle formation. Tian et al.[13-15] studied the dynamic ice accretion process on the engine blades during rotation through ice wind tunnel experiments and analyzed the impact of ice accretion on the performance of the engine's fan blades. Experimental results demonstrated that the formed ice layers correspond well to the original shapes of the fan blades under the rime icing condition. Meanwhile, the surface of the spinner and fan blades could grow out needle-shaped icicles rapidly under the glaze icing condition.

To investigate the icing process of rotating components in aero-engines, it is necessary to accurately calculate the impact characteristics of supercooled water droplets. Accordingly, some researchers have conducted corresponding studies. Bidwell[16] proposed the mixing plane analogy for calculating the flow of ice particles in turbo-machinery and applied it to analyze the trajectories, temperature changes, and phase changes of ice particles with diameters of 5, 20, and 100 μm. Wu et al.[17] explored the water droplets' impingement characteristics and heat transfer within the blade passages of the Rotor67 using the multiple reference frame (MRF) method and made preliminary predictions on icing conditions. Simulation results indicated a general increase in the collection efficiency with the increase in droplet diameter. Tan et al.[18] utilized the Eulerian method to calculate the droplet impingement characteristics on the engine spinner and fan blades. The distribution of liquid water content and droplet collection efficiency for different droplet sizes were also obtained. It was found that the large droplets primarily impinged on the concave surface of the fan blades, while relatively small droplets tended to impinge on the bypass duct and core duct. Gao et al.[19] simulated the impact of droplet impingement characteristics on the three different shapes of aero-engine spinners using the Eulerian method with a rotating coordinate system and analyzed the effects of different factors on the water collection efficiencies. The findings suggested that the impact region extended across the entire windward surface of the conical spinner. However, in the case of the elliptical and coniptical spinner, the impact region only covered the windward surface prior to the position of the impingement limit. Nevertheless, these researchers only conducted numerical simulation studies on the droplet impingement characteristics without further icing calculations.

Researchers have recently focused on predicting the icing phenomenon on rotating components through numerical simulations. Mu et al.[20-21] proposed a three-dimensional numerical simulation to investigate water film shedding on rotating cowling. This study found that the icing area and ice mass decreased due to increased rotation speed. In addition, in the case of the angle of attack, the rotation enhanced ice accumulation and significantly affected the uniformity of ice accretion. Jian et al.[22] also conducted numerical research on the water film flow

and shedding of the rotating spinner. They found that when the rotational speed and inflow velocity increased, the proportion of water film detachment increased, resulting in a decrease in total ice mass. Guo et al.[23] developed an unsteady icing model for three-dimensional rotating surfaces based on the shallow-water icing model. They applied this model to the simplified rotating blade for icing calculation. The results showed that the icing and water film coverage areas deviated more significantly with the increased rotational speed. Furthermore, the icing and water film coverage areas gradually increased with the increase of water droplet diameter. While these studies represent important contributions to the field, they have yet to address several key issues: (1) The limited studies simulating icing on full-scale engine windward components; (2) insufficient research on engine icing issues under supercooled large droplet conditions; (3) the lack of a systematic understanding for three-dimensional simulation of ice accretion on surfaces under rotational conditions.

Based on the above issues, this study aims to construct the complete full-scale engine entry components and perform ice accretion calculations. This model will be subsequently compared and validated with experimental results. To solve the supercooled large droplets (SLD) dynamic behavior, the corresponding droplet dynamic models will be introduced to calculate droplet impingement characteristics. In addition, the results of 3D icing on the windward components of the engine under freezing drizzle conditions in Appendix O of the Federal Aviation Regulations will be explored. The current work aims to accumulate technical reserves for subsequent simulation studies and provide data support for designing anti/de-icing systems.

1 Numerical Method

This study undertakes consideration of the engine fan blade rotation, and the main methods to realize the flow simulation under the rotation of rotating components include the single reference frame (SRF) method, the MRF method, the mixing plane method (MPM) and the sliding mesh method (SMM)[24]. The MRF method exhibits high efficiency and reduces the computational cost[25-26]. Thus, it is implemented in this study to solve the fluid flow and heat transfer of the rotating components.

The methodology[27-28] utilized in this study for ice accretion simulation using the MRF method is as follows. The air flow field is calculated using the MRF method. The cylindrical space consisting of the rotating blades and the spinner is regarded as the rotational zone, which is solved with the moving reference frame equations. On the other hand, the irrotational zone outside the cylindrical space is treated using stationary frame equations. Furthermore, the droplet impingement and ice accretion calculations are solved within the stationary frame.

The numerical simulation of ice accretion involves three essential steps: Air flow field calculation, droplet impingement calculation, and ice accretion calculation. In this section, the numerical method including the governing equations of the icing process, the solution procedure and the main solving method, is introduced and validated through the comparison with the experimental data in literatures.

1.1 Air flow field calculation

The droplet's dynamic motion and heat transfer phenomena are intimately linked to the flow field. Consequently, aerodynamic analysis of the airflow field is warranted as a prerequisite step. The air flow field is calculated utilizing the MRF model. The pressure-based solver of the commercial software Ansys Fluent is chosen to solve the Reynolds-averaged Navier-Stokes (RANS) equations. The Realizable k-ε model is employed as the turbulence model, and the scalable wall function is adopted to capture the details at the boundary layer. The continuity equation, momentum equation, energy equation, turbulent kinetic energy term, and turbulent dissipation rate term use the second-order upwind for spatial discretized. The semi-implicit method for pressure-linked equations (SIMPLE) is used to process the coupling of pressure and velocity.

The governing equations of air flow for the

moving reference frame can be written as

$$\frac{\partial \rho_a}{\partial t}+\nabla\cdot\left(\rho_a \boldsymbol{u}_a\right)=0 \tag{1}$$

$$\frac{\partial\left(\rho_a \boldsymbol{u}_a\right)}{\partial t}+\nabla\cdot\left(\rho_a \boldsymbol{u}_a\otimes \boldsymbol{u}_a\right)=-\nabla p+\nabla\cdot\boldsymbol{\tau}-2\rho_a(\boldsymbol{\omega}\times \boldsymbol{u}_a)-\rho_a\boldsymbol{\omega}\times(\boldsymbol{\omega}\times \boldsymbol{r}) \tag{2}$$

$$\frac{\partial\left(\rho_a E\right)}{\partial t}+\nabla\cdot\left(\rho_a \boldsymbol{u}_a H\right)=\nabla\cdot(k\nabla T+\boldsymbol{\tau}\cdot\boldsymbol{u}_a) \tag{3}$$

where ρ_a is the air density, $\boldsymbol{u}_a$ the air velocity in relative frame of reference, p the static pressure and $\boldsymbol{\tau}$ the stress tensor. The Coriolis and centrifugal force are added to the left end of the momentum equation. Here $\boldsymbol{\omega}$ is the rotational velocity, $\boldsymbol{r}$ the distance from the axis of rotation, E and H are the relative internal energy and relative total enthalpy, respectively, and k the thermal conductivity.

1.2 Droplet impingement calculation

Based on the results for the flow field, it is necessary to solve the droplet impingement characteristics. The Eulerian approach holds significant advantages, given its ability to accurately calculate the dynamic behavior of droplets on complex surfaces. In this study, the Eulerian method[29] adopted in the software Ansys FENSAP-ICE is employed to analyze the droplet impingement dynamics. This methodology treats the supercooled droplet as a continuum and introduces the droplet volume fraction to establish the continuity and momentum equations. It is noteworthy that, due to the distinctive motion characteristics of supercooled large droplets, it is necessary to utilize dynamic models to modify the Eulerian model of the droplet impingement process and accurately analyze and simulate the impact characteristics.

1.2.1 Governing equations

The droplet continuity and momentum equations are expressed as

$$\frac{\partial \alpha}{\partial t}+\nabla\cdot(\alpha \boldsymbol{u}_d)=0 \tag{4}$$

$$\frac{\partial(\alpha \boldsymbol{u}_d)}{\partial t}+\nabla\cdot\left(\alpha \boldsymbol{u}_d\otimes \boldsymbol{u}_d\right)=\frac{C_D Re_d}{24K}\alpha(\boldsymbol{u}_a-\boldsymbol{u}_d)+\alpha\left(1-\frac{\rho_a}{\rho_d}\right)\frac{\boldsymbol{g}}{Fr^2} \tag{5}$$

where α is the droplet volume fraction, $\boldsymbol{u}_d$ the droplet velocity, K the inertial parameter for droplets, C_D the drag coefficient of a droplet, Re_d the droplet Reynolds number, ρ_d the droplet density, $\boldsymbol{g}$ the gravity vector, and Fr the Froude number. The first term on the right side of Eq.(5) represents the drag, and the second one is buoyancy and gravity.

The droplet Reynolds number, the inertial parameter and the Froude number are specifically expressed as

$$Re_d=\frac{\rho_a d U_{a,\infty}\left\|\boldsymbol{u}_a-\boldsymbol{u}_d\right\|}{\mu_a} \tag{6}$$

$$K=\frac{\rho_d d^2 U_{a,\infty}}{18 L_\infty \mu_a} \tag{7}$$

$$Fr=\frac{\left\|U_{a,\infty}\right\|}{\sqrt{L_\infty g}} \tag{8}$$

where $U_{a,\infty}$ is the free stream velocity, d the droplet diameter, μ_a the air dynamic viscosity, and L_∞ the characteristic length.

The governing equations are solved using the Galerkin finite element discretization scheme[30] to obtain the droplet volume fraction and the droplet velocity. Then the droplet collection efficiency can be calculated as an input parameter for ice accretion calculation.

1.2.2 Large droplet dynamic models

Because of the complexity of the dynamic behavior of supercooled large droplets, conventional assumptions for ordinary-sized droplets are deemed unsuitable. Therefore, it is imperative to account for the effects of terminal droplet velocity, droplet deformation and breakup, and droplet-wall interactions, including splash and bounce phenomena. Fig.1 shows the motion behavior of a supercooled large droplet. To ensure a precise simulation of the dynamic behavior of SLD, the terminal velocity model, the deformation and breakup model, and the splash and rebound model are employed.

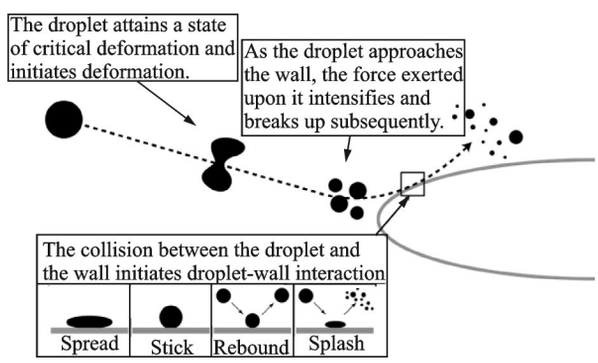

Fig.1 Supercooled large droplets' dynamic behavior

(1) Terminal velocity model

The effect of gravity on supercooled large droplets is a non-negligible factor, given their large diameters, ultimately causing the droplets to fall with a terminal velocity. Khan and Richardson[31] have deduced an equation that establishes such a correlation between the terminal Reynolds number and the Galileo number as

$$Re_{\mathrm{t}}=\left(2.33Ga^{0.018}-1.53Ga^{-0.016}\right)^{13.3} \tag{9}$$

Utilizing the obtained terminal Reynolds number, the corresponding terminal velocity may be calculated by

$$\boldsymbol{u}_{\mathrm{t}}=\frac{\mu_{\mathrm{a}}Re_{\mathrm{t}}}{\rho_{\mathrm{a}}dU_{\mathrm{a},\infty}} \tag{10}$$

$$\boldsymbol{u}_{\mathrm{d}}=\begin{Bmatrix}u_{\mathrm{d}}\\ v_{\mathrm{d}}\\ w_{\mathrm{d}}\end{Bmatrix}=\begin{Bmatrix}u_{\mathrm{d-t}}+g_x\|\boldsymbol{u}_{\mathrm{t}}\|\\ v_{\mathrm{d-t}}+g_y\|\boldsymbol{u}_{\mathrm{t}}\|\\ w_{\mathrm{d-t}}+g_z\|\boldsymbol{u}_{\mathrm{t}}\|\end{Bmatrix} \tag{11}$$

where $\{u_{\mathrm{d-t}}, v_{\mathrm{d-t}}, w_{\mathrm{d-t}}\}$ represents the initial droplet velocity vector and $\{g_x, g_y, g_z\}$ the gravitational unit vector.

(2) Deformation and breakup model

Supercooled large droplets experience a twofold influence from aerodynamic shear force and surface tension during the course of their movement. However, owing to their relatively sizable diameter, an imbalance ensues between droplet surface tension and aerodynamic shear force. The self-surface tension becomes insufficient to resist the aerodynamic shear force, resulting in the collapse of the droplets' spherical configuration. Accordingly, changing from a spherical shape to an oblate disk shape or even breaking into a number of small-sized droplets may arise.

When applied to deformed supercooled large droplets, the drag model traditionally employed for spherical droplets is inadequate. To address this issue, Clift et al.[32] proposed an extended drag model to account for the increased aerodynamic drag under SLD conditions as

$$C_{\mathrm{D}}=\begin{cases}fC_{\mathrm{D,sphere}}+(1-f)C_{\mathrm{D,disk}} & We_{\mathrm{b}}\leqslant 12\\ C_{\mathrm{D,disk}} & We_{\mathrm{b}}>12\end{cases} \tag{12}$$

$$f=1-\left(1+0.07\sqrt{We_{\mathrm{b}}}\right)^{-6} \tag{13}$$

where $C_{\mathrm{D,sphere}}$ is the drag coefficient of a spherical droplet, $C_{\mathrm{D,disk}}$ the drag coefficient of an oblate disk droplet, and We_{b} the breakup Weber number.

Upon attaining a sufficient aerodynamic shear force, the surface tension fails to maintain the structural integrity of droplets, causing the disintegration of the supercooled large droplets into many smaller stable droplets. Étude et al.[33] proposed the following equation that tracks the variation of droplet size during the breakup process.

$$\frac{Dd}{Dt}=\frac{\partial d}{\partial t}+\boldsymbol{u}_{\mathrm{d}}\cdot\nabla d=\frac{d_{\mathrm{stab}}-d_{\mathrm{o,b}}}{T} \tag{14}$$

where $d_{\mathrm{o,b}}$ is the pre-breakup droplet diameter. The droplet breakup mechanisms established by Pilch and Erdman[34] determine nondimensional breakup time T and define the subcritical breakup Weber number to be approximately 12. It is only when the Weber number of a droplet exceeds this value that fragmentation will occur. d_{stab} is the stable droplet diameter at the point of complete cessation of all forms of breakup activities.

$$d_{\mathrm{stab}}=\frac{12\sigma}{\rho_{\mathrm{a}}U_{\mathrm{a},\infty}^2\|\boldsymbol{u}_{\mathrm{a}}-\boldsymbol{u}_{\mathrm{d}}\|^2} \tag{15}$$

where σ is the droplet surface tension.

(3) Rebound and splash model

When supercooled large droplets come into contact with a surface, they interact with it primarily by spreading, sticking, rebounding and splashing. The splash and rebound behaviors have a more pronounced effect, although all of them contribute to the overall droplet collection efficiency. The occurrence of splash behavior can be determined through the splash judgment criterion developed by Trujillo et al.[35], which is based on the Cossali splashing parameter[36].

$$K_{\mathrm{C}}>540R^{-0.35} \tag{16}$$

where R represents the ratio between the surface roughness and the diameter of the impinging droplet.

The post-impact droplets diameter is determined by

$$d_{\mathrm{s}}=8.72\mathrm{e}^{-0.0281K_{\mathrm{M}}}d_{\mathrm{o,s}} \tag{17}$$

The ratio between the post-impact droplet diameter and pre-impact droplet diameter is constrained to a range between 0.05 and 1. K_{M} is the Mundo splashing parameter.

The number of secondary droplet fragments is

written as Eq.(18), and its range is $n_s \leqslant 1\,000$.

$$n_s = 1.676 \times 10^{-5} K_M^{2.539} \tag{18}$$

The post-splash local water collection efficiency can be obtained by correcting the original local water collection efficiency.

$$\beta_s = \left[1 - n_s\left(\frac{d_s}{d_{o,s}}\right)^3\right]\beta_o \tag{19}$$

The rebound behavior is judged according to the model of Bai and Gosman[37], where rebound behavior occurs if the droplet impact Weber number is in the range of $2 < We_s < 10$.

1.3 Ice accretion calculation

Once the results of the flow field and the droplet impingement characteristics are obtained, the ice accretion calculation can be performed. The shallow water icing model[38] employed in Ansys FENSAP-ICE is based on the Messinger model[39]. This model is also adopted for icing prediction in this study. The corresponding mass and energy equations are solved to derive the ice accretion result. The finite volume method based on the cell center is chosen for solving these governing equations[40].

Mass conservation

$$\rho_w\left[\frac{\partial h_f}{\partial t} + \nabla\cdot(\boldsymbol{u}_f h_f)\right] = U_{a,\infty}\mathrm{LWC}\beta - \dot{m}_{evap} - \dot{m}_{ice} \tag{20}$$

where ρ_w is the density of water, h_f the water film height, $\boldsymbol{u}_f$ the water film speed, and LWC the liquid water content. The right side of Eq.(20) is the mass flux of droplet impingement, evaporation and solidification, respectively.

The water film speed is defined as

$$\boldsymbol{u}_f = \frac{h_f}{2\mu_w}\boldsymbol{\tau} - \frac{h_f^2}{3\mu_w}\rho_w \boldsymbol{a} \tag{21}$$

where μ_w is the water dynamic viscosity, $\boldsymbol{\tau}$ the surface shear stress vector, and $\boldsymbol{a}$ the cumulative accelerations the water film is subjected to.

Energy conservation

$$\rho_w\left[\frac{\partial h_f C_w \tilde{T}}{\partial t} + \nabla\cdot\left(\boldsymbol{u}_f h_f C_w \tilde{T}\right)\right] = \left[C_w \tilde{T}_{d,\infty} + \frac{\|\boldsymbol{u}_d\|^2}{2}\right]U_{a,\infty}\mathrm{LWC}\beta - 0.5\left(L_{evap} + L_{subl}\right)\dot{m}_{evap} + \left(L_{fus} - C_{ice}\tilde{T}\right)\dot{m}_{ice} + \varepsilon\sigma\left(T_\infty^4 - T^4\right) + \dot{Q}_h \tag{22}$$

where C_w and C_{ice} are the specific heat of water and ice, respectively; $\tilde{T}$ is the equilibrium temperature, L_{evap} the latent heat of evaporation, L_{subl} the latent heat of sublimation, L_{fus} the latent heat of fusion, and $\dot{Q}_h$ the convective heat flux. The first three terms on the right side of Eq.(22) are the heat transfer generated by the impinging supercooled water droplets, by evaporation and by ice accretion.

Close the system according to the compatibility relations

$$h_f \geqslant 0,\ \dot{m}_{ice} \geqslant 0,\ h_f\tilde{T} \geqslant 0,\ \dot{m}_{ice}\tilde{T} \leqslant 0 \tag{23}$$

1.4 Validation

Due to the limited published data regarding whole aero-engine icing, the verification is carried out in this paper based on the working parameters in Ref.[41] with the rotating spinner as the calculation object. Fig.2 shows the spinner model given in Ref.[41]. It has a conical angle of 60° and a bottom diameter of 412 mm. A favorable agreement between the two sets of data is observed by comparing the simulation result with experimental data on ice accretion. It validates the reliability of the 3D icing prediction method employed in this study. Table 1 and Fig.3 exhibit the calculation parameters and comparative findings. In Fig.3, the parameter "d" of the coordinate axis represents the bottom diameter of the

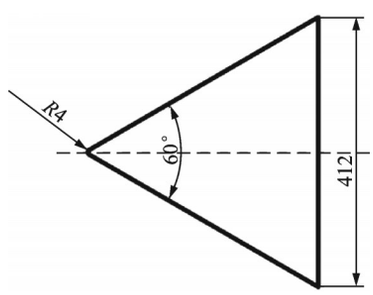

Fig.2 The spinner model

Table 1 Test conditions for method validation

Parameter	Value
Freestream temperature/K	263
Freestream velocity/(m•s^{-1})	65
Rotational speed/(r•min^{-1})	2 000
Liquid water content/(g•m^{-3})	0.3
Median volume diameter/μm	50
Total time of ice accretion/s	335

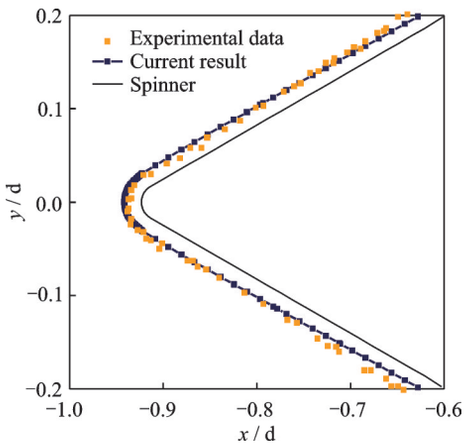

Fig.3 Ice shape comparison between experimental result and current work

spinner model.

2 Calculation Condition

2.1 Geometry and grid

The rotating wide-chord swept-back fan blades represent the primary site of supercooled water droplet icing, yet airfoils often replace these blades for computational purposes. Although such an approach reduces the computational complexity, it simultaneously disregards the influence of the blades' shape on the surrounding flow field. Consequently, this study focuses on the full-scale entry components of a turbofan engine, which contains upper and lower inlet lips of varying thickness, a spinner with a 60° cone angle, and 24 wide-chord swept-back blades distributed in a circumferential formation.

With a view to the reliability of the calculation results and reducing the influence of the outer boundary on the flow field near the windward side of the engine, the distance from the upstream far-field boundary to the inlet lip is set to 21 times the fan diameter, and the distance from the surrounding far-field boundary to the engine is set to 15 times the fan diameter; the trailing edge of the engine casing is extended to downstream of the calculation domain, and the extension distance is 30 times the fan diameter. The computational domain and the grid are shown in Fig.4, and the locations of circumferential sections at $\theta=0°$, 90°, 180°, and 270° are marked.

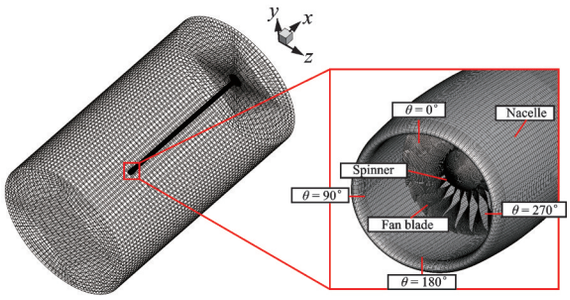

Fig.4 Computational domain and the grid

2.2 Grid independence

To ensure the accuracy of the calculations, five meshes are selected for the grid sensitivity analysis. The corresponding numbers of cells are 8 488 857, 9 084 080, 10 016 839, 11 152 357, and 12 158 611, respectively. The calculations are performed at the following conditions: 65 m/s freestream velocity, 263 K freestream temperature, and 79.54 kPa freestream pressure. The relationship between the total number of cells and the drag coefficient, as well as the pressure distribution around the circumferential section $\theta=0°$ of the engine inlet lip, are shown in Fig.5. As the number of cells increases, the drag coefficients of the three finer grids exhibit

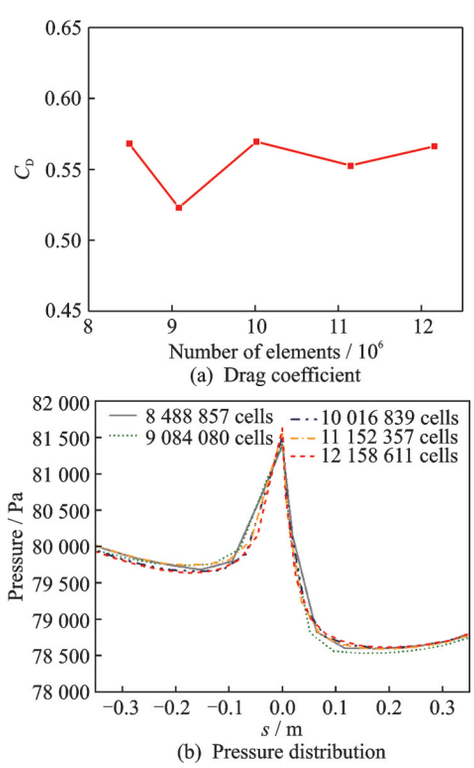

Fig.5 Grid independence results of drag coefficient and pressure distribution at circumferential section $\theta=0°$

less variation. The horizontal coordinate in Fig.5(b) is the normalized form so that those greater than zero represent the outer edge of the inlet, and those less than zero are the inner edge of the inlet. The pressure distribution trend of the five grids is consistent, and the pressure predicted by the rougher two grids is slightly larger. Therefore, the mesh with 10 016 839 cells is employed in the present study to reduce time and ensure the calculation accuracy.

2.3 Operating condition

The current work aims to investigate the phenomenon of ice accretion on the engine's inlet components under the fan's rotational effect. To establish realistic conditions for the study, typical rotational speeds of the engine fan are adopted. Liquid droplets in high-altitude clouds differ in size, and using a monodisperse distribution is inconsistent with the actual icing environment. Thus, the icing and the droplet distribution calculation conditions are determined based on the freezing drizzle conditions in Appendix O of the Federal Aviation Regulations. The specific flight conditions, meteorological environment, and droplet distribution are listed in Table 2 and Table 3.

Table 2 Droplet distribution

Droplet diameter/μm	252.0	163.0	97.0	48.0	36.0	29.0	23.0	18.0	13.0	9.0
Weight/%	2.5	2.5	5	5	5	10	20	20	20	10

Table 3 Operating condition parameters

Parameter	Value
Freestream temperature/K	263
Freestream velocity/(m•s^{-1})	65
Freestream pressure/Pa	79 540
Rotational speed/(r•min^{-1})	0 / 2 000 / 4 100
Liquid water content/(g•m^{-3})	0.3
Total time of ice accretion/s	335

3 Results and Discussion

3.1 Droplet impingement characteristics

The supercooled droplet impingement can be obtained by the Eulerian method under various rotational speed conditions. As shown in Fig.6, the principal impact regions of water droplets are in the vicinity of the inlet lip stagnations, the spinner leading edge points, and the windward side of the blades. The variation of the local droplet collection efficiency β on the inlet lip shows a similar trend. At different rotational speeds, the values of β are larger near the inlet lip stagnation and gradually decrease to zero along the inner and outer surfaces of the nacelle, respectively. The effects of rotation cause the impact regions of droplets on the fan blades to experience varying degrees of movement. Moreover, the area of the maximum droplet collection efficiency gradually shifts toward the lower regions of the blades. With the increasing rotational speed, the droplet collection efficiency exhibits a generally increasing trend. This situation may be attributed to

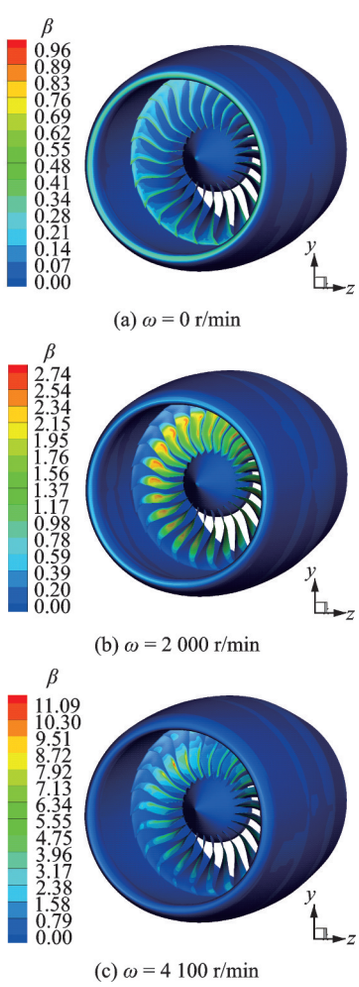

Fig.6 Local water collection at different rotational speeds

the rotation of the fan blades driving the air and liquid droplets around the engine to the inside of the engine. The higher the rotational speed, the more significant the amount of droplets drawn in by the engine, resulting in enhanced engine water collection capacity. Due to its central symmetry, the spinner exhibits comparatively low variation in the water droplet collection efficiency.

Fig.7 illustrates the local water collection efficiency distributions at the engine inlet lip and spinner for different rotational speeds. The water collection efficiency on the inlet lip demonstrates an increase in value with the increasing rotational speed of the blades. This result is consistent with the findings in Refs.[42-43] that the increased intake air flow rate led to an increase in the water collection efficiency. Simultaneously, there have been observable shifts in the maximum value of the water collection efficiency and the impingement limit. On the inlet lip, the water collection efficiency distribution curves at the locations of four circumferential sections have also tilted toward the outer surface direction. There is an increase in the degree of shift with the increase in rotational speed. The water collection efficiencies at the spinner's two cross sections increase with the rotational speed increase. However, the water droplet impingement limit remains consistent compared to that of the stationary case. The distribution curves of water collection efficiencies exhibit a concave shape at positions on the posi-

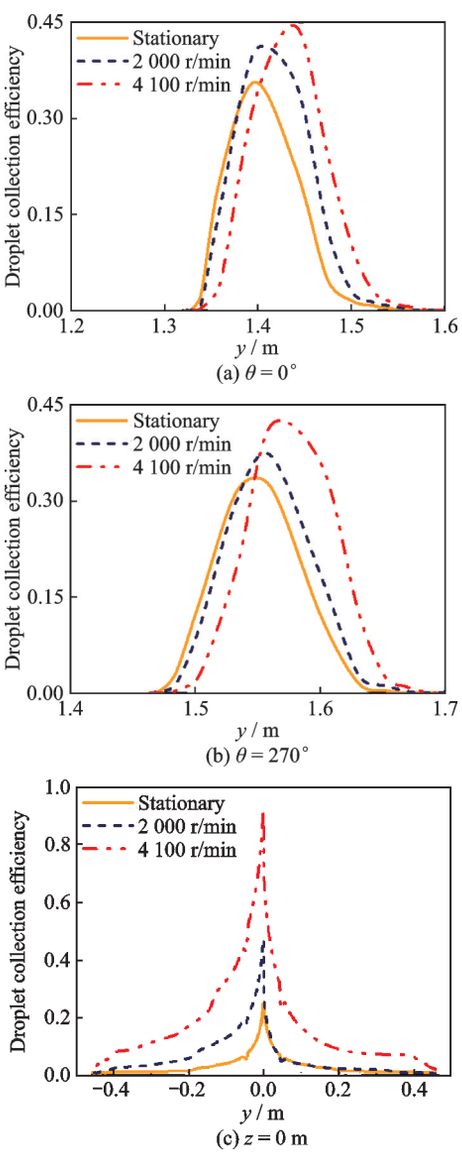

Fig.7 Local water collection efficiency of engine inlet lip and spinner at different rotational speeds

tive y-axis and negative z-axis of the central line of the spinner. These irregular water collection efficiencies might result from the spinner's rotation and gravity's impact on the supercooled large droplets.

Due to the uniform droplet impingement and icing characteristics of fan blades corresponding to the four circumferential sections, the blade located at the position illustrated in Fig.8 is chosen for further investigation. Moreover, the locations of cross-sections at different blade heights are marked. The variation in water collection efficiencies at different sections of blade heights with modifications in rotational speed is depicted in Fig.9. Under the influence of rotation, the water collection efficiency distributions revealed new peaks near the center of different blade heights. A profound investigation of the droplet velocity distribution at the center of the blade section with different heights shows a dramatic burst in droplet velocity. This significant increase in the velocity of droplets at this location may be attributed to the turbulence disturbances between adjacent blades under rotation, and the droplets' own kinetic energy. With an increase in rotational speed, the turbulence kinetic energy around the rotating blades increases, leading to a considerable variation in the airflow direction near the blades and making it more favorable for droplets to collide at this location. Furthermore, the incoming airflow provides the droplets with greater kinetic energy, resulting in a sharp increase in droplet velocity at this position. This high droplet velocity condition leads to a significant surge in the local water collection efficiency at that location. The droplet velocity distributions of the blade root are shown in Fig.10. At the cross sections of the blade root and the middle of the blade, the rotational effect causes the rangeof droplet impact to expand. However, the range of droplet impact at rotational conditions diminishes compared to the static case at the top position of the blade. The

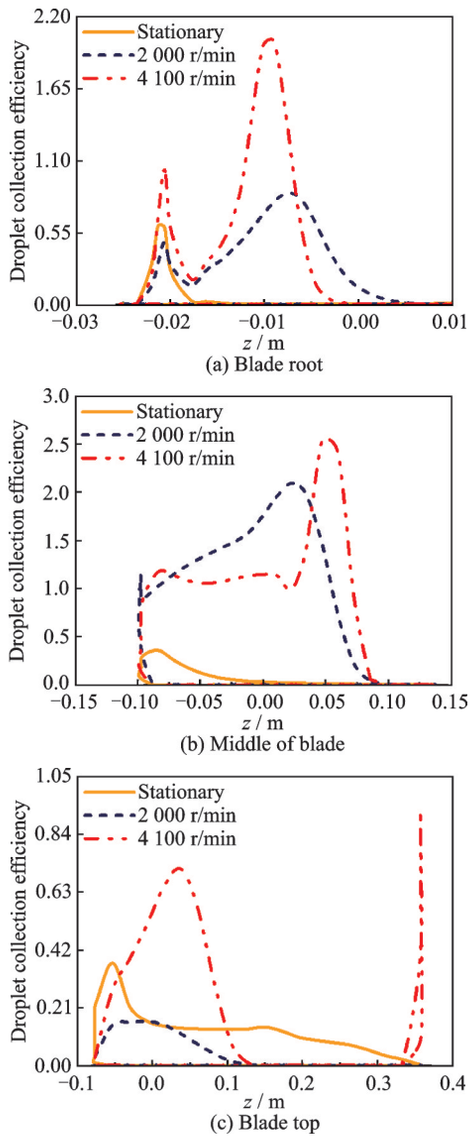

Fig.9 Comparison of water collection efficient of different rotational speeds at different blade heights

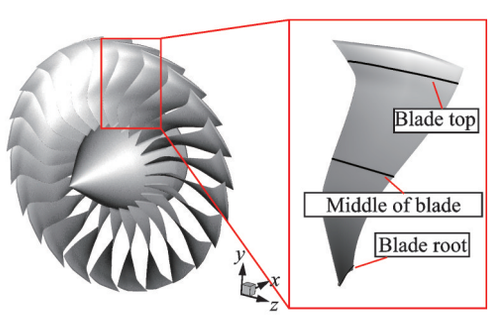

Fig.8 Cross sections of different blade heights

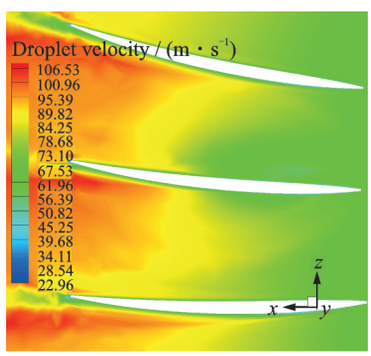

(a) ω = 0 r/min

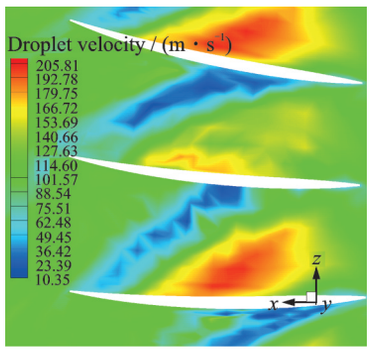

(b) ω = 2 000 r/min

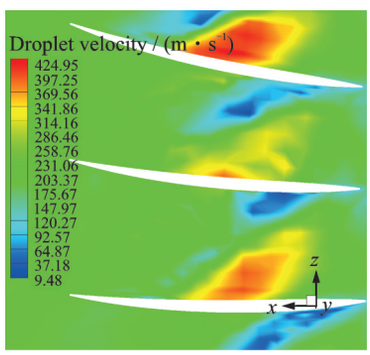

(c) ω = 4 100 r/min

Fig.10 Droplet velocity distribution of different rotational speeds at the blade root

small range of the vehement increase in the water collection efficiency at the trailing edge of the blade top could be due to the tangential velocity caused by the rotation.

3.2 Ice accretion characteristics

The corresponding three-dimensional icing regions at different rotational speeds can be seen in Fig.11. The results indicate that, for the three rotational speeds tested, the icing areas on the inlet lip are constant. However, as the rotational speed increases, the icing region on the blade decreases. The icing accumulation mainly occurs near the blade root. Moreover, the flow passages in front of the fans experience ice accretion under rotation, and the icing area increases with the rotational speed. These

(a) ω = 0 r/min

(b) ω = 2 000 r/min

(c) ω = 4 100 r/min

Fig.11 Icing regions at different rotational speeds

findings suggest that the increased rotational speed may mitigate the ice accretion tendency on the fan blade but lead to more significant icing accumulation in the duct area. That should be considered in the design and operation of the fan.

The results of the ice shape and ice thickness on the inlet lip and the spinner are presented in Fig.12. As the rotational speed increases, the ice

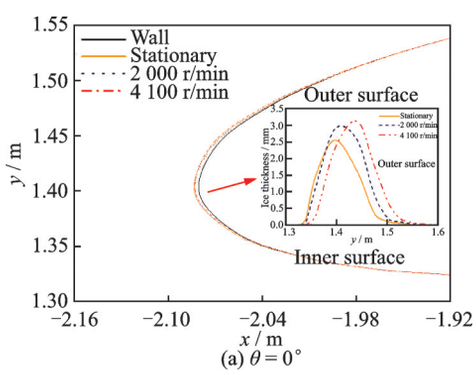

(a) θ = 0°

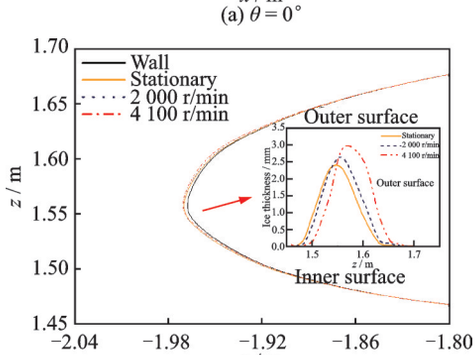

(b) θ = 270°

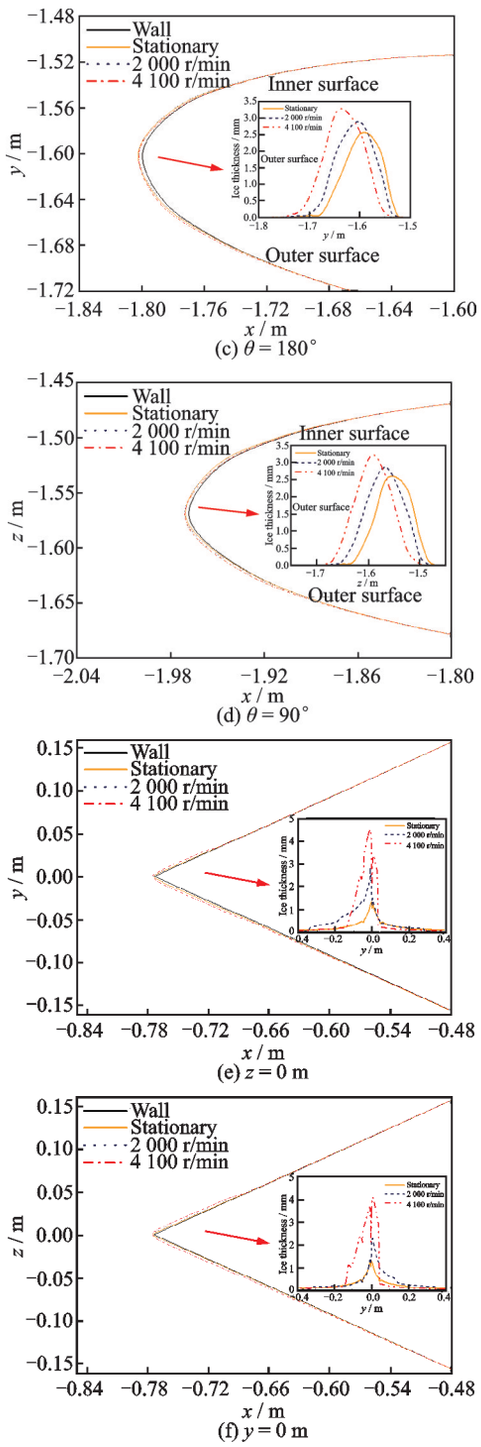

Fig.12 Ice shape and ice thickness of engine inlet lip and spinner at different rotational speeds

thickness on the outer surface of the inlet lip gradually becomes greater than that on the inner surface. Moreover, the location of the maximum ice thickness on the inlet lip shifts towards the outer surface with the increase in rotational speed. The ice shape of the spinner exhibits a greater thickness in the negative y-axis and positive z-axis directions, corresponding to the previously described droplet impingement characteristics. The ice thicknesses at these locations under rotational conditions are generally greater than that of the stationary case. Furthermore, the ice thickness on the inlet lip and the spinner exhibits an increasing trend as the rotational speed increases. This finding agrees with the preceding variation of the water collection efficiency that results from the increased intake air flow rate. At the rotational speed of 2 000 r/min, the maximum ice thickness on the engine inlet lip shows an increase of 13% compared to that observed at the same location under the stationary condition. Similarly, at the rotational speed of 4 100 r/min, the maximum ice thickness on the inlet lip shows an increase of 27% compared to the stationary condition. In addition, on the spinner, the maximum ice thickness at 2 000 r/min increases by 1.17 times compared to the stationary condition. At 4 100 r/min, the maximum ice thickness on the spinner increases by 2.46 times compared to the stationary condition.

Fig.13 shows the ice shapes of different rotational speeds at different blade heights. As shown in Fig.13, with the increase in rotational speed, the ice accumulation at the location of the blade root decreases. The ice accretion on the blades is mainly concentrated at the blade roots' leading edge and windward side, wherein the ice thickness of these locations is notably greater in comparison to the upper regions of the blades. This observation can be attributed to the larger water collection efficiencies and lower temperature at the blade roots, which significantly affect the icing characteristics along the blades. Conversely, the upper regions of the blades exhibit higher water collection efficiency but also higher temperature, thereby reducing the likelihood of ice accretion. The stationary blade's ice accretion predominates at the leading edge on the windward side of the blade root. The location of the maximum ice thickness moves backwards from the windward side with increased rotational speed, ultimately accumulating at the center of the windward side on the blade root.

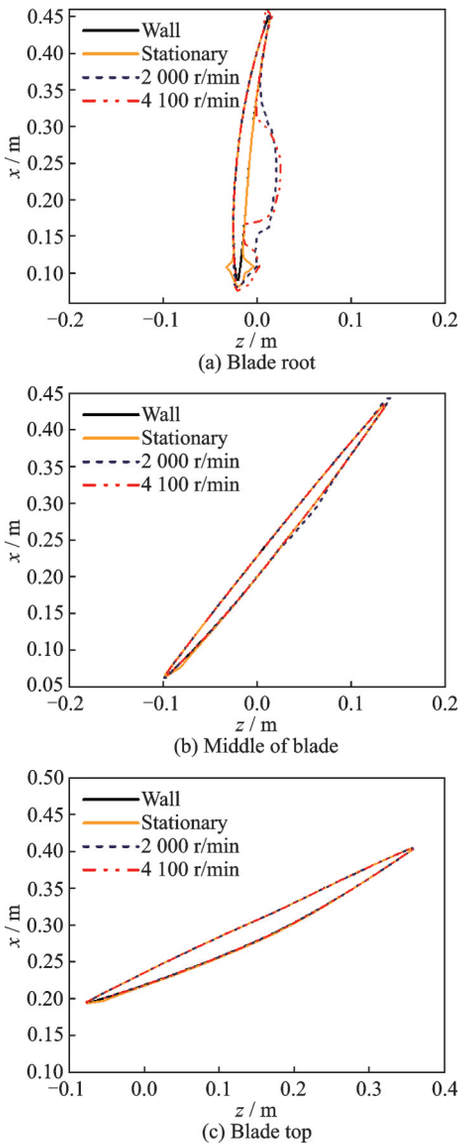

Fig.13 Comparison of ice shapes of different rotational speeds at different blade heights

4 Conclusions

This study employs the MRF model to consider the rotational effect, while taking into account the dynamic characteristics of terminal velocity, deformation, breakup, splash, and rebound of supercooled large droplets. The impacts of rotational speed on the droplet impingement characteristics and ice accretion characteristics on engine inlet components under the supercooled large droplet condition are investigated. The main conclusions are as follows:

(1) The rotation has significant influences on the water collection efficiency of the engine inlet lip and the spinner. With increasing rotational velocity, the water collection efficiency of these locations increases, and the collection efficiency curve of the inlet lip shifts to the outer surface of the inlet lip. Meanwhile, the droplet impingement area on the top of the blade tends to decrease, while there is a significant increase in the water collection efficiency at the blade's middle section.

(2) Ice accumulates primarily on the inlet lip, the front part of the spinner, and the windward side of the blade. The icing area of the inlet lip and the spinner remains unchanged overall as the rotational speed increases, while the icing area on the blades' windward side decreases. In addition, under rotation, the icing area of the blade occurs mainly at the blade's root, while the upper part of the blade exhibits minimal ice accretion. This observation can be attributed to the relatively higher temperatures near that location.

(3) The maximum ice thickness on the inlet lip and the spinner increases with the increase of the rotational speed. On the inlet lip, the maximum ice thickness at 2 000 r/min and 4 100 r/min increases by 13% and 27% compared to the stationary condition, respectively. Moreover, on the spinner, the maximum ice thickness at 2 000 r/min and 4 100 r/min increases by 1.17 and 2.46 times compared to the stationary condition, respectively.

References

[1] TETTEH E, LOTH E, NEUTEBOOM M O, et al. In-flight gas turbine engine icing: Review[J]. AIAA Journal, 2022, 60(10): 5610-5632.

[2] LIU Zhe, BAI Jie, ZHANG Wenjun. Statistical analysis of aviation flight accidents caused by dangerous weather[J]. Journal of Civil Aviation Flight University of China, 2022, 33(1): 23-27. (in Chinese)

[3] PAPADAKIS M, YEONG H W, WONG S C, et al. Comparison of experimental and computational ice shapes for an engine inlet[C]//Proceedings of AIAA Atmospheric and Space Environments Conference. Toronto, Ontario, Canada: AIAA, 2010: 7671-7710.

[4] SHEN X, LIN G, YU J, et al. Three-dimensional numerical simulation of ice accretion at the engine inlet[J]. Journal of Aircraft, 2013, 50(2): 635-642.

[5] LI J, LIU Z, ZHANG L, et al. Research on numerical simulation of glaze ice for aircraft and aero-engine entry components[C]//Proceedings of the 2018 Asia-Pacific International Symposium on Aerospace Technology (APISAT 2018). Singapore: Springer, 2019: 579-590.

[6] ZHU Q, GUAN N. Numerical simulation of icing

characteristics on the surface of an aero-engine guide blade[C]//Proceedings of Journal of Physics: Conference Series. [S.l.]: IOP Publishing, 2023, 2442(1): 012027.

[7] YANG Q, GUO X, DONG W, et al. Ice accretion and aerodynamic effects on a turbofan engine nacelle under takeoff conditions[J]. Aerospace Science and Technology, 2022, 126: 107571-107584.

[8] ZHENG M, GUO Z, DONG W, et al. Experimental investigation on ice accretion on a rotating aero-engine spinner with hydrophobic coating[J]. International Journal of Heat and Mass Transfer, 2019, 136: 404-414.

[9] HU Y, XU C, LI S, et al. Experimental study on icing and anti-icing of a rotating conical spinner[J]. Applied Thermal Engineering, 2023, 219: 119373.

[10] MUROOKA T, SHISHIDO S, HIRAMOTO R, et al. Surface coating effect on protection of icing for axial fan blade: SAE Technical Paper[R].[S.l.]: SAE, 2011.

[11] ZHANG Lifen, GE Xin, ZHANG Fei, et al. An ice wind tunnel test study on the scaling law of a rotating cone[J]. Journal of Experiments in Fluid Mechanics, 2021, 35(4): 52-59. (in Chinese)

[12] LI L, LIU Y, HU H. An experimental study on dynamic ice accretion process over the surfaces of rotating aero-engine spinners[J]. Experimental Thermal and Fluid Science, 2019, 109: 109879.

[13] LI L, LIU Y, HU H. An experimental study of the dynamic ice accreting process over a rotating aero-engine fan model[C]//Proceedings of 2018 Atmospheric and Space Environments Conference. Atlanta, USA: AIAA, 2018: 3013.

[14] TIAN L, LI L, HU H, et al. An experimental study on the dynamic ice accretion process over the surfaces of the rotating fan blades of an aero-engine model[C]//Proceedings of AIAA SCITECH 2022 Forum. San Diego, CA & Virtual: AIAA, 2022: 2435.

[15] TIAN L, LI L, HU H, et al. Experimental study of dynamic ice accretion process over rotating aeroengine fan blades[J]. Journal of Thermophysics and Heat Transfer, 2023,37(2): 353-364.

[16] BIDWELL C S. A Lagrangian parcel based mixing plane method for calculating water based mixed phase particle flows in turbo-machinery[J]. Computational Particle Mechanics, 2015, 2(1): 39-50.

[17] WU T, YANG Q, GUO Z, et al. Supercooled water droplet impingement and icing region prediction on a rotating fan blade[C]//Proceedings of AIAA Aviation 2019 Forum. Dallas, Texas: AIAA, 2019: 3309-3322.

[18] TAN Y, WEI W. Numerical study of super-cooled droplet impingement on aeroengine[J]. Mechanics, 2020, 26(1): 25-30.

[19] GAO X, QIU B, WANG Z, et al. Influence of spinner shape on droplet impact over rotating spinners[J]. Aerospace, 2023, 10(1): 68-89.

[20] MU Z, SHEN X, LIN G, et al. Numerical simulation for ice accretion on rotating cowling considering water film shedding[C]//Proceedings of the 54th AIAA Aerospace Sciences Meeting. [S.l.]: AIAA, 2016: 2187.

[21] MU Z, LIN G, BAI L, et al. 3D numerical simulation of ice accretion on a rotating surface[J]. International Journal of Aeronautical and Space Sciences, 2017, 18(2): 352-364.

[22] JIAN Jinjin, JI Honghu, CAO Guangzhou, et al. Numerical study on water film flow and shedding in ice accretion of rotating spinner[J]. Journal of Aerospace Power, 2018, 33(11):2725-2736. (in Chinese)

[23] GUO Qi, SHEN Xiaobin, LIN Guiping, et al. Numerical simulation of icing on aircraft rotating surfaces[J]. Journal of Beijing University of Aeronautics and Astronautics, 2022, 48(11): 2259-2269. (in Chinese)

[24] SADREHAGHIGI I. Essentials of turbo machinery in CFD[M]. Annapolis, USA:CFD Open Series, 2018.

[25] ANSYS, Inc. ANSYS fluent-theory guide-release 2022R1[M]. Canonsburg, USA: ANSYS Inc.,2022.

[26] LANE G L, SCHWARZ M P, EVANS G M. Comparison of CFD methods for modelling of stirred tanks[C]//Proceedings of the 10th European Conference on Mixing. [S.l.]:Elsevier Science, 2000: 273-280.

[27] YI Xian, WANG Kaichun, MA Honglin, et al. 3-D numerical simulation of droplet collection efficiency in large-scale wind turbine icing[J]. ACTA Aerodynamica Sinica, 2013, 31(6): 745-751. (in Chinese)

[28] YI Xian, WANG Kaichun, MA Honglin, et al. Computation of icing and its effect of horizontal axis wind turbine[J]. ACTA Energiae Solaris Sinica, 2014, 35(6): 1052-1058. (in Chinese)

[29] BOURGAULT Y, HABASHI W, DOMPIERRE J, et al. An Eulerian approach to supercooled droplets impingement calculations[C]//Proceedings of the 35th Aerospace Sciences Meeting and Exhibit. Reno, USA: AIAA, 1997: 176-187.

[30] BOURGASULT Y, HABASHI W, DOMPIERRE J, et al. A finite element method study of Eulerian droplets impingement models[J]. International Journal for Numerical Methods in Fluids, 1999, 29(4): 429-449.

[31] KHAN A R, RICHARDSON J F. The resistance to motion of a solid sphere in a fluid[J]. Chemical Engineering Communications, 1987, 62(1/2/3/4/5/6): 135-150.

[32] CLIFT R, GRACE J R, WEBER M E. Bubbles, drops, and particles[M]. New York: Academic Press,

1978.
[33] Étude L B. Implémentation des phénomènes d'éclatement de gouttes d'eau dans un écoulement diphasique[R]. Paris: Rapport de Stage de Fin d'Étude, Institut Scientifique Polytechnique Galilée, 2003.
[34] PILCH M, ERDMAN C A. Use of breakup time data and velocity history data to predict the maximum size of stable fragments for acceleration-induced breakup of a liquid drop[J]. International Journal of Multiphase Flow, 1987, 13(6): 741-757.
[35] TRUJILLO M F, MATHEWS W S, LEE C F, et al. Modelling and experiment of impingement and atomization of a liquid spray on a wall[J]. International Journal of Engine Research, 2000, 1(1): 87-105.
[36] COSSALI G E, COGHE A, MARENGO M. The impact of a single drop on a wetted solid surface[J]. Experiments in Fluids, 1997, 22(6): 463-472.
[37] BAI C X, GOSMAN A D. Development of methodology for spray impingement simulation[J]. SAE Technical Paper Series, 1995, 104: 69-87.
[38] BOURGAULT Y, BEAUGENDRE H, HABASHI W G. Development of a shallow-water icing model in FENSAP-ICE[J]. Journal of Aircraft, 2000, 37(4): 640-646.
[39] MESSINGER B L. Equilibrium temperature of an unheated icing surface as a function of air speed[J]. Journal of the Aeronautical Sciences, 1953, 20(1): 29-42.
[40] BEAUGENDRE, H A PDE-based 3D approach to in-flight ice accretion[D]. Montreal: McGill University, 2003.
[41] CHEN N, JI H, HU Y, et al. Experimental study of icing accretion on a rotating conical spinner[J]. Heat and Mass Transfer, 2015, 51(12): 1717-1729.
[42] SHEN Xiaobin, LIN Guiping, YANG Shenghua. Analysis on three dimensional water droplets impingement characteristics of engine inlet[J]. Journal of Beijing University of Aeronautics and Astronautics, 2011, 37(1): 1-5. (in Chinese)
[43] YAO Hong, NING Yijun. Effect of air inflow of engine on impingement characteristics of water droplets at leading edge[J]. Journal of Shenyang University of Technology, 2016, 38(6): 645-650. (in Chinese)

Acknowledgements This work was supported by the National Natural Science Foundation of China (No.51902256) and the Aeronautical Science Foundation of China (No. 2020Z057053002). The authors would like to thank Mr. XIA Quanzhong from Sichuan Gas Turbine Establishment of Aero Engine Corporation of China for supporting the calculation.

Author Dr. **FU Zaiguo** received his Ph.D. degree from Tokyo University of Science in 2015. He is an associate professor in Shanghai University of Electric Power. His current research interests include complex fluid flow, heat and mass transfer, and multi-field in combustor of gas turbine.

Author contributions Dr. **FU Zaiguo** designed the study, reviewed and revised the manuscript. Mr. **FENG Wenjie** completed the calculations, conducted analysis, and wrote and revised the manuscript. Ms. **WANG Zijing** reviewed and edited the original draft. Dr. **LIU Bin** contributed to funding acquisition and reviewed the original draft. All authors commented on the manuscript draft and approved the submission.

Competing interests The authors declare no competing interests.

(Production Editor: WANG Jing)

发动机进口旋转部件的三维积冰数值模拟

付在国[1], 冯文杰[1], 王子婧[1], 刘 斌[2]
(1.上海电力大学能源与机械工程学院,上海 201306,中国; 2.西北工业大学航空学院,西安 710072,中国)

摘要:飞机在过冷大水滴条件下运行时,受科里奥利力和离心力作用的发动机旋转部件会表现出与静止部件不同的积冰特性。本文考虑了过冷大水滴的终端沉降速度、变形破碎和飞溅反弹动力学特性,并采用多重参考坐标系方法处理旋转条件下的流动和传热,对发动机进口部件包括进气道唇口、整流罩和风扇叶片的液滴撞击及积冰特性进行了三维数值模拟。转速为0、2 000和4 100 r/min情况下的模拟结果表明,随着转速的增加,进气道唇口上的积冰从唇口内表面向其外表面移动。此外,旋转叶片上的积冰主要集中在叶片根部位置,且积冰量随转速增加而减少。进气道唇口和整流罩上的冰层厚度随转速的增加而增加,转速为4 100 r/min下的进气道唇口和整流罩上的最大积冰厚度与静止状态相比分别增加了0.27倍和2.46倍。此项工作能够为后续的防/除冰技术发展提供参考。

关键词:航空发动机;三维结冰预测;过冷大水滴;旋转叶片;数值模拟